

Unveiling intrinsic bulk photovoltaic effect in atomically thin ReS₂

Maria Ramos^{1}, Tanweer Ahmed¹, Bao Q. Tu¹, Eleni Chatzikyriakou², Lucía Olano-Vegas¹,
Beatriz Martín-García^{1,4}, M. Reyes Calvo^{3,4}, Stepan S. Tsirkin^{2,4}, Ivo Souza^{2,4}, Félix
Casanova^{1,4}, Fernando de Juan^{4,5}, Marco Gobbi^{2,4*}, Luis E. Hueso^{1,4*}*

¹CIC nanoGUNE BRTA, 20018 Donostia-San Sebastián, Basque Country, Spain

²Centro de Física de Materiales CSIC-UPV/EHU, 20018 Donostia-San Sebastián, Basque
Country, Spain

³BCMaterials, Basque Center for Materials, Applications and Nanostructures, UPV/EHU
Science Park, 48940 Leioa, Spain

⁴IKERBASQUE, Basque Foundation for Science, 48009 Bilbao, Basque Country, Spain

⁵Donostia International Physics Center, 20018 Donostia-San Sebastián, Basque Country,
Spain

*Correspondence to: m.ramos@nanogune.eu, marco.gobbi@ehu.eus,
l.hueso@nanogune.eu

KEYWORDS: bulk photovoltaics, intrinsic photocurrent, second-order conductivity, broken inversion symmetry

ABSTRACT. The bulk photovoltaic effect (BPVE) offers a promising avenue to surpass the efficiency limitations of current solar cell technology. However, disentangling intrinsic and extrinsic contributions to photocurrent remains a significant challenge. Here, we fabricate high-quality, lateral devices based on atomically thin ReS₂ with minimal contact resistance, providing an optimal platform for distinguishing intrinsic bulk photovoltaic signals from other extrinsic photocurrent contributions originating from interfacial effects. Our devices exhibit large bulk photovoltaic performance with intrinsic responsivities of ~1 mA/W in the visible

range, without the need for external tuning knobs such as strain engineering. Our experimental findings are supported by theoretical calculations. Furthermore, our approach can be extrapolated to investigate the intrinsic BPVE in other non-centrosymmetric van der Waals materials, paving the way for a new generation of efficient light-harvesting devices.

MAIN TEXT. The exploitation of high-order, nonlinear photocurrents could potentially overcome the fundamental efficiency limit of current solar cells based on p-n junctions (1) (2) (3). This limit, known as the Shockley-Queisser limit, is directly related to the active material's bandgap. It dictates a maximum theoretical efficiency of about 33.7% for a single junction under standard conditions (4) (5). While multi-junction solar cells can achieve higher efficiencies, they remain restricted by the bandgaps of their constituent materials, limiting the utilization of lower-energy parts of the spectrum. Nonlinear photocurrents, unconstrained by bandgap limitations, present a feasible alternative to unlock the full potential of the solar spectrum and surpass the efficiency limit, extending light utilization into the infrared and beyond (6) (7) (8) (9).

The proportionality relation between second-order photocurrents and an applied electric field (or light polarization) in a material is dictated by the nonlinear conductivity tensor $\sigma^{(2)}$, which is determined by the material's symmetry. Breaking inversion symmetry is essential for the emergence of second-order photocurrents, leading to what is commonly referred to as "bulk" photovoltaic effect (BPVE). These terms reflect the characteristics of this phenomenon: the generation of a net DC photocurrent upon illumination of a single, homogenous material at zero applied bias.

While the discovery of the BPVE originated from research on ferroelectric perovskite oxides (10) (11) (12) (13) (14) (15) (16) (17), these materials have not been considered a viable solution against traditional solar cell technology due to their low light-to-electrical power conversion efficiency. Alternatively, van der Waals (vdW) materials present straightforward strategies for breaking inversion symmetry, offering a new and exciting avenue for BPVE research (18) (19) (20) (21) (22) (23) (24) (25) (26) (27) (28). Especially, vdW polar materials

have demonstrated large responsivities on the order of 1-10 mA/W when implemented in vertical device architectures (29) (30) (31) (32) (33).

Among various promising vdW materials, ReS₂ emerges as a particularly attractive candidate for BPVE exploration. While bulk ReS₂ is centrosymmetric (34) (35), numerous studies highlighted the polytypism in the material (36) (37). Different stacking orders of the distorted 1T crystal structure (known as 1T') can lead to broken symmetries, particularly in the few-layer limit of ReS₂ where stacking energetics can differ from that of bulk samples. This broken symmetry is crucial for the emergence of several nonlinear phenomena such as second harmonic generation (SHG), as demonstrated by Song *et al.* (38), and ferroelectricity, as confirmed by Wan *et al.* (39) in few-layer ReS₂. These findings suggest the potential for a significant BPVE in few-layer ReS₂. Earlier reports on BPVE in ReS₂ have observed photocurrents at zero applied bias only at grain boundaries in polycrystalline flakes (40), or solely at the crystalline edge of heterostructures formed by two ReS₂ flakes (41). Furthermore, Wang *et al.* (42) reported BPVE in single-crystalline ReS₂ flakes using a vertical device geometry.

Nonetheless, vertical geometries face challenges in the identification of the intrinsic BPVE. A key challenge in BPVE research lies in distinguishing nonlinear photocurrents from those generated at Schottky barriers within a device. This differentiation is crucial, as the Schottky barrier photovoltaic effect can dominate the overall photocurrent, questioning whether the responsivity has an intrinsic origin. Lateral geometries with a focused incoming beam enable spatial separation of intrinsic and extrinsic effects, facilitating detection of photocurrents from the pristine, active material without ambiguity. However, sizeable BPVE signals under normal incidence excitation in lateral devices using non-centrosymmetric transition metal dichalcogenides usually require the application of external tuning knobs, such as strain (43) (44).

In this work, we overcome the limitations found across the literature by employing an optimal device engineering technique, which enables to clearly identify the BPVE in thin, single-crystalline ReS₂ flakes without the need of external tuning knobs or vertical device architectures. Our approach utilizes a lateral device geometry where the ReS₂ layer is in

contact with graphite electrodes and encapsulated between hexagonal boron nitride (hBN). This yields devices with minimal contact resistance, reducing electrode-interface photocurrents and providing an optimal platform for sensitive detection of intrinsic non-linear photocurrents. We demonstrate the BPVE in ReS_2 by studying the dependence of the observed photocurrent on the incoming light polarization and its spatial distribution across the device. Remarkably, our approach enables the detection of a large BPVE response in ReS_2 , with intrinsic responsivities of $\sim 1\text{mA/W}$. These experimental values are seconded by our calculated photocurrent response based on a non-centrosymmetric bilayer structure. Additionally, our fabrication approach can potentially be extrapolated to the study of the BPVE in other non-centrosymmetric vdW materials with no perpendicular two-fold rotational axis, where in-plane photocurrents are generically allowed even at normal incidence.

A critical aspect of successfully measuring a BPVE signal is employing a device design that minimizes unwanted effects and maximizes the contribution of the “intrinsic”, active material. To achieve this, we employ a device fabrication with the following considerations: First, a lateral device geometry is chosen to separate the BPVE from other potential photovoltaic effects originating at interface between different materials, which are typically present in devices with vertical geometries. Second, the ReS_2 active layer is sandwiched in between two thin hBN flakes to minimize surface defects and prevent any influence from the substrate. Third, few-layer graphite flakes are used as electrodes in contact with ReS_2 to minimize contact resistance. Fourth, a pick-up technique is employed during the device assembly to ensure clean interfaces between all materials. Further details about device fabrication are provided in section S1.

Fig. 1a-b summarizes the different vdW layers present in the devices through simplified sketches from both 3D and cross-sectional viewpoints, respectively. A bilayer-thick ReS_2 flake serves as the active channel, contacted by two thin graphite electrodes and encapsulated between top and bottom hBN flakes (see section S2 for ReS_2 thickness estimation). The vdW stack illustrated in Fig. 1a-b is placed onto a $\text{SiO}_2/\text{Si}^{++}$ substrate.

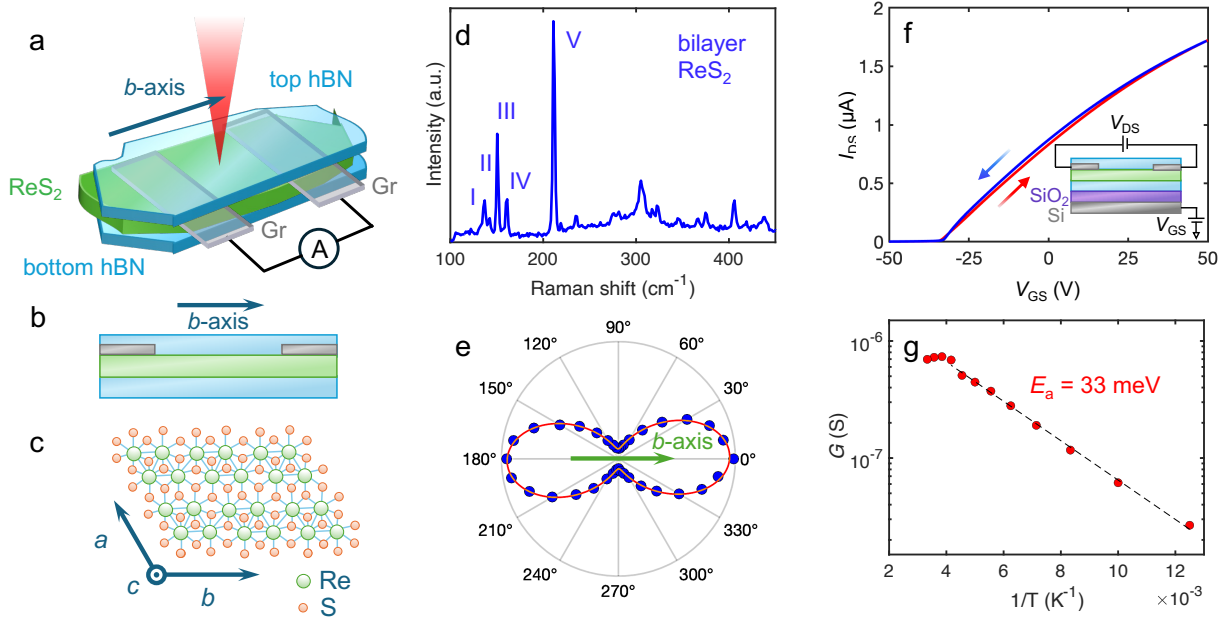


Figure 1. Simplified three-dimensional (a) and cross-sectional (b) device schemes showing the different vdW layers composing the system. The color coding chosen for each material layer in panel b is the same as for panel a. In panel a, a CW (continuous wave) laser is used to illuminate the device, while a current meter reads the photogenerated current. (c) Top-view atomic configuration of a monolayer ReS_2 with $1T'$ structure. (d) Raman spectrum of a bilayer ReS_2 , where the first five vibrational modes can be clearly identified. (e) Polar plot of the A_g -like active Raman mode at $\sim 212 \text{ cm}^{-1}$ (mode V in panel d). The orientation of the Re-Re bonds (b -axis) is identified along the maximum intensity. (f) Back- and forth-transfer curves of one of the fabricated devices, upon back-gate voltage (see sketch in the inset) and in dark conditions for $V_{DS} = 0.2 \text{ V}$. (g) Arrhenius plot for the conductance, where a linear fit to the data yields an activation energy of 33 meV .

The top-view atomic configuration of a monolayer ReS_2 with $1T'$ structure is shown in Fig. 1c, where Re-Re bonds form chains along the b -axis. The unit cell of ReS_2 contains four rhenium atoms and eight sulfur atoms, with the a and b axes forming an angle of 118° (34) (35). As indicated in panels a and b of Fig. 1, current detection is carried out along the b -axis of the ReS_2 flakes, as the crystals are naturally cleaved along this crystallographic direction. This is also confirmed through polarization-resolved Raman spectroscopy of the vibrational mode V ($\sim 212 \text{ cm}^{-1}$). As mode V involves out-of-plane vibrations of S atoms coupled with in-plane vibrations of Re atoms along the b -axis, a beam polarized along the direction of the Re atomic chain optimally couples with the in-plane vibrational component of the V mode.

Consequently, the polarization at which the intensity of mode V is maximum indicates the orientation of the b -axis (see Fig. 1d-e).

To ensure the quality and functionality of the fabricated devices, we check the transfer characteristics of a representative device (see Fig. 1f). These measurements reveal a well-defined on/off switching ratio of $\sim 10^3$ and a field-effect mobility of $12 \text{ cm}^2/(\text{V}\cdot\text{s})$, indicating good quality and efficient carrier transport in agreement with previous reports (45). In addition, the transfer curves exhibit very small hysteresis, suggesting minimal charge trapping effects within the device.

Low contact resistance is essential for detecting second-order photocurrents. Our graphite electrodes minimize Schottky barriers, enabling efficient carrier extraction. This is confirmed by the low activation energy of our device, $E_a = 33 \text{ meV}$ (see Fig. 1g), significantly lower than ReS_2 devices contacted to traditional metals (46) (47).

With the optimized ReS_2 devices in hand, we next investigate their intrinsic photovoltaic response. To do this, different $I_{\text{DS}}-V_{\text{DS}}$ curves in dark conditions and under illumination are studied. During the measurement, a linearly polarized laser emitting at 633 nm is used to illuminate the ReS_2 channel at different excitation powers. To avoid any photocurrent contribution from the $\text{ReS}_2/\text{graphite}$ interface, the laser beam is tightly focused to a $\sim 1 \mu\text{m}$ spot size onto the center of the ReS_2 channel, whose length exceeds $5 \mu\text{m}$.

The current-voltage characteristics shown in Fig. 2a under dark conditions follow a linear trend, evidencing low contact resistance (see section S3 for larger applied voltages). Upon illumination, the $I_{\text{DS}}-V_{\text{DS}}$ curves exhibit a significant displacement that increases with the optical excitation power. This displacement indicates the generation of photocurrent at zero applied bias (short-circuit current, I_{SC}) and a non-zero voltage at zero current (open-circuit voltage, V_{OC}). These parameters define the operating regime of the device under illumination, where light-to-electrical power conversion occurs.

The values of the short-circuit current and the open-circuit voltage from Fig. 2a are shown respectively in Fig. 2b-c as a function of the excitation power. Both I_{SC} and V_{OC} exhibit a linear dependence on the excitation power (P_{opt}). This is indicative of a second-order photocurrent

generation process, since power scales proportionally to the square of the electric field ($P_{\text{opt}} \propto |E|^2$).

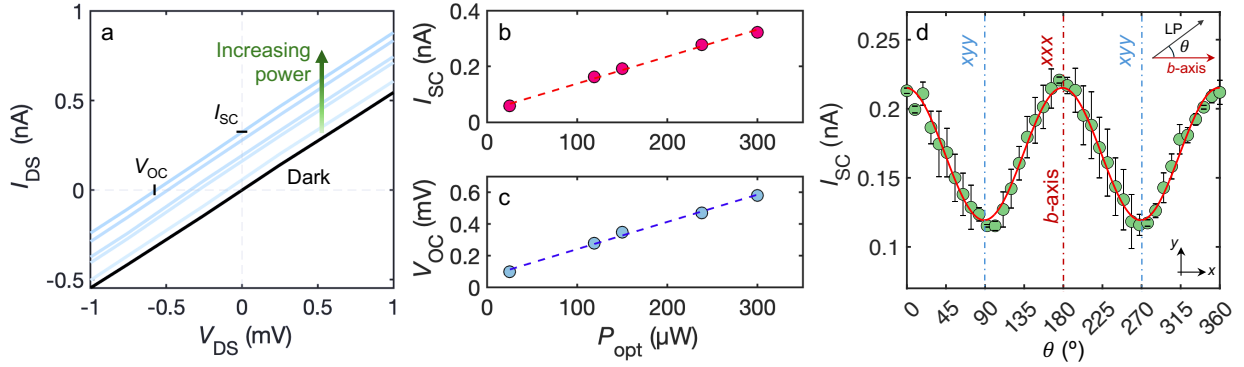


Figure 2. (a) $I_{\text{DS}}-V_{\text{DS}}$ characteristics of the ReS_2 device in the dark and upon illumination powers from 30 to 300 μW at 633 nm wavelength. (b) Short-circuit current extracted from panel a. (c) Open-circuit voltage obtained from panel a. (d) Angular dependence of the short-circuit current measured along the b -axis as a function of the linear polarization of the incoming light. The top right inset indicates the relative angle θ between the crystallographic b -axis of ReS_2 and the linear polarization of light (LP). Here, the b -axis is aligned with the x -coordinate (this happens at $\theta = 0^\circ, 180^\circ, 360^\circ$). Measurements are carried out with an excitation wavelength of 633 nm for an optical power of 120 mW.

A characteristic feature of a BPVE current is its sensitivity to the linear polarization of the incident light, whose response can be understood from the nonlinear conductivity $\sigma^{(2)}$ describing the material's response. To investigate this, we measured the short-circuit current at different angles of the linearly polarized light with respect to the b -axis of ReS_2 . The results are shown in Fig. 2d, where the green dots represent the experimental data and the error bars indicate the standard deviation for each measurement. The results confirm a strong correlation between the short-circuit current and the light polarization, with a photocurrent approximately $2\times$ larger when the light polarization aligns with the b -axis of ReS_2 .

Interestingly, while the photocurrent exhibits a clear periodic modulation with light polarization, it remains non-zero for any polarization orientation. This agrees with previous observations of non-vanishing SHG for all polarization angles in ReS_2 (38) since these two effects are determined by the inherent crystal symmetry of ReS_2 . Moreover, the non-zero mean photocurrent reveals a polar nature for ReS_2 crystals.

The results in Fig. 2d can be described by an equation capturing the relationship between a second-order photocurrent density along a given i -direction and the non-linear conductivity tensor as a quadratic electric field response:

$$j_i^{\text{BPVE}} = \sigma_{ijk}^{(2)} E_j E_k \quad (1)$$

where $\sigma_{ijk}^{(2)}$ is the second-order conductivity and E_j , E_k are the components of the applied electric field along j and k , which in our case correspond to the electric field direction of the incoming light wave (or light polarization).

Since photocurrent is directly measured during experiments, from here onwards we provide the equations in terms of total photocurrent (I) and not photocurrent density (j). In our experiments, both the electric field (or light polarization) and the photocurrent detection are restricted to an in-plane configuration. Consequently, tensor components like those describing current flow along the z -axis can be disregarded. Also, since the photocurrent detection takes place along the b -axis of ReS_2 , we adopt a convention where the b -axis aligns with the x -coordinate direction of our experimental setup. Therefore, the equation describing the photocurrent simplifies to:

$$I_x = t \cdot r (\sigma_{xxx}^{(2)} E_x^2 + \sigma_{xyy}^{(2)} E_y^2 + 2\sigma_{xxy}^{(2)} E_x E_y) \quad (2)$$

where t is the ReS_2 thickness and r is the beam radius. Considering an electric field amplitude E_0 forming an angle θ with respect to the x -axis, the electric field components can be written as $E_x = E_0 \cos \theta$ and $E_y = E_0 \sin \theta$. For a Gaussian beam, the electric field amplitude can be written in terms of optical power as $E_0^2 = 4P_{\text{opt}} / (nc\epsilon_0\pi r^2)$, where n is the refractive index of ReS_2 , c is the speed of light and ϵ_0 is the vacuum permittivity. Substituting these expressions into eq. 2, the photocurrent as a function of the polarization angle becomes:

$$I_x = 4 \frac{t \cdot P_{\text{opt}}}{\pi n c \epsilon_0 r} (\sigma_{xxx}^{(2)} \cos^2 \theta + \sigma_{xyy}^{(2)} \sin^2 \theta + 2\sigma_{xxy}^{(2)} \cos \theta \sin \theta) \quad (3)$$

A fit of the polarization dependent photocurrent in Fig. 2d using eq. 3 yields nonlinear conductivity values of $\sigma_{xxx}^{(2)} = (5.51 \pm 0.07) \text{ mA/V}^2$, $\sigma_{xyy}^{(2)} = (3.06 \pm 0.07) \text{ mA/V}^2$ and $\sigma_{xxy}^{(2)} = (-0.05$

± 0.06) mA/V² within a 95% confidence interval. Further details on the fitting parameters used in this analysis are provided in section S4 of the Supporting Information.

To compare with other works, the responsivity of the device can be obtained from Fig. 2d. Since the responsivity is directly influenced by the sample dimension, a normalization based on sample size is needed for accurate comparisons across different studies. The “intrinsic” responsivity of our device is calculated from Fig. 2d as the ratio of the photocurrent density to the laser power density: $\kappa = (J^{\text{BPVE}}/I_{\text{opt}})$, where $J^{\text{BPVE}} = \langle I_{\text{SC}} \rangle / (r \cdot t)$ and $I_{\text{opt}} = P_{\text{opt}} / (\pi \cdot r^2)$ being $\langle I_{\text{SC}} \rangle$ the mean photocurrent, r the laser beam radius, t the ReS₂ thickness and P_{opt} the optical power. For our bilayer device, this yields a BPVE intrinsic responsivity of 1.3 mA/W.

We employed scanning photocurrent microscopy (SPCM) to detect variations in the device’s photovoltaic response across different regions. Fig. 3a shows an optical microscope image of a representative device with a four-layer ReS₂ active channel. The corresponding SPCM maps are shown in Fig. 3b-c, obtained under different illumination wavelengths and excitation powers, with zero applied bias. Both SPCM maps exhibit a remarkable similarity in the spatial distribution of the photogenerated current across the ReS₂ device for the two excitation wavelengths. The SPCM maps show a photocurrent with opposite sign at the lateral contact regions, located at both ends of the ReS₂ channel. The dominant mechanism of this photocurrent is a photovoltaic effect due to a built-in electric field at the graphite/ReS₂ interface. Here, the source (drain) barrier drives photogenerated electrons (holes) towards the semi-metal contact, resulting in a positive (negative) photocurrent. Furthermore, the SPCM maps also reveal a photocurrent generated within the ReS₂ channel.

The corresponding transverse profiles are respectively depicted in Fig. 3d-e, displaying a distinct and sharp increase in current when the ReS₂ active channel is illuminated. This rise indicates efficient photocurrent generation within the ReS₂ channel itself and its magnitude exhibits a direct proportionality to the illumination power used for excitation.

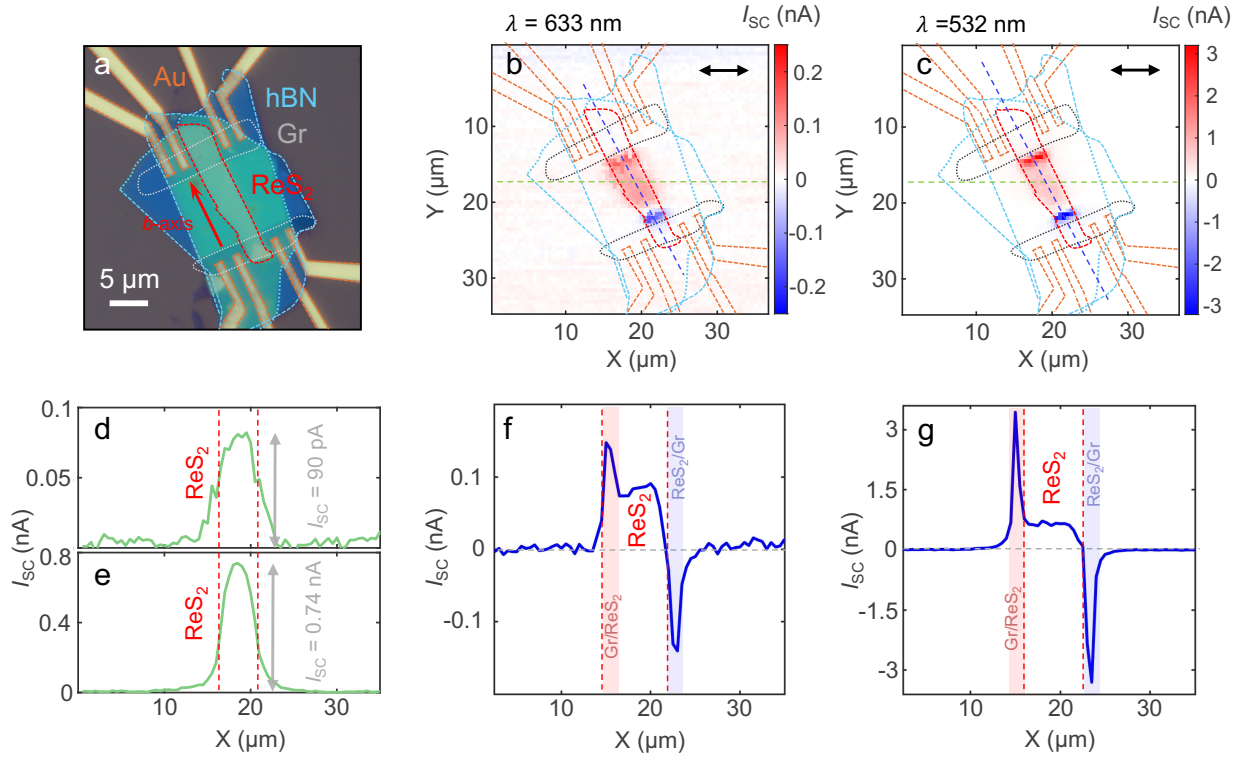


Figure 3. (a) Optical microscope image of a ReS₂ device. (b)-(c) Scanning photocurrent maps of the device shown in panel a for excitation wavelengths of 633 nm and 532 nm at excitation powers of 30 μ W and 400 μ W, respectively. The color scale represents the photocurrent intensity, with red and blue colors indicating positive and negative photocurrents, respectively. The black, double arrows at the top, right-hand side indicate the orientation of the linear polarization of light. (d)-(e) Transverse line profiles obtained from the photocurrent maps shown in panels b and c, respectively. (f)-(g) Longitudinal line profiles extracted from the photocurrent maps in panels b and c, respectively, where the reddish and blueish areas indicate positive and negative photocurrents built at the lateral Schottky barriers between the active channel and the graphite contacts.

While the transverse profiles focus on current fluctuations across the ReS₂ channel, the longitudinal profiles track the current along the ReS₂ active layer. The data obtained from the longitudinal line profiles in Fig. 3f-g provides valuable insights into the different contributions to the overall photocurrent signal. A constant dark current or noise level can be identified when the device is illuminated in non-photoresponsive regions. The photocurrent built at the lateral semi-metal/semiconductor interface appears at the edges of the ReS₂ channel with opposite sign contributions, with an extension of ~ 2 - μ m. Finally, in the central area of the device, the bulk photovoltaic current generated along the ReS₂ channel can be distinguished.

Significantly, the longitudinal line profiles reveal a disparity in the scaling behavior between the photovoltaic current built at the lateral semi-metal/semiconductor interface and that originating from the pristine ReS₂ flake, supporting the distinct origins of the two signals. Moreover, the magnitude of the photocurrent originated along the pristine ReS₂ flake in the longitudinal line profiles is consistent with the photocurrent intensity observed in the transverse line profiles. The uniformity of this signal across the SPCM maps and its sharp rise in the line profiles further support the dominance of the BPVE as the mechanism for photocurrent generation in our device.

Interestingly, we are not able to discern any BPVE signal in lateral ReS₂ devices fabricated with traditional metal contacts, such as prepatterned Ti/Au electrodes, as confirmed by the absence of any photocurrent at zero bias originated at the pristine ReS₂ channel through SPCM maps. Moreover, the Schottky barrier photocurrent is an order of magnitude greater than that observed in our graphite-contacted devices (see section S5 of the Supporting Information).

The device characterized in Fig. 3 exhibits intrinsic responsivities of 1.6 and 1.0 mA/W at wavelengths of 633 and 532 nm, respectively, for a ReS₂ channel containing four layers. Our low-contact-resistance devices outperform similar lateral devices characterized under analogous experimental conditions, where unstrained non-centrosymmetric 3R- and 2H-MoS₂ exhibited negligible BPVE currents (43) (44).

While bulk ReS₂ is centrosymmetric (34) (35), different stacking orders of the 1T' crystal structure can lead to broken symmetries in the few-layer limit. Recent works have pointed out the existence of a bilayer stacking different from the bulk one, where the top monolayer is rotated by 180° with respect to the bottom one. This generically leads to a non-centrosymmetric structure which is ferroelectric (39) and displays SHG (48), being also expected to generate a BPVE current.

We have performed an *ab initio* calculation of the non-linear conductivity in the non-centrosymmetric state defined in Ref. (39), using Wannier functions derived from first principles simulations (49) (see section S1 for details).

The response tensor $\sigma_{ijk}^{(2)}$ was calculated from:

$$\sigma_{ijk}^{(2)}(0, \omega, -\omega) = -\frac{i\pi e^3}{4\hbar^2} \int [d\mathbf{k}] \sum_{n,m} f_{nm} (I_{mn}^{abc} + I_{mn}^{acb}) [\delta(\omega_{mn} - \omega) + \delta(\omega_{nm} - \omega)] \quad (4)$$

where I_{kmn}^{abc} is the product of the interband dipole matrix and its generalized derivative with respect to the crystal momentum, $f_{nm} = f_n - f_m$ are Fermi occupation factors and $\hbar\omega_{nm} = E_m - E_n$ is the difference between the energies of bands n and m .

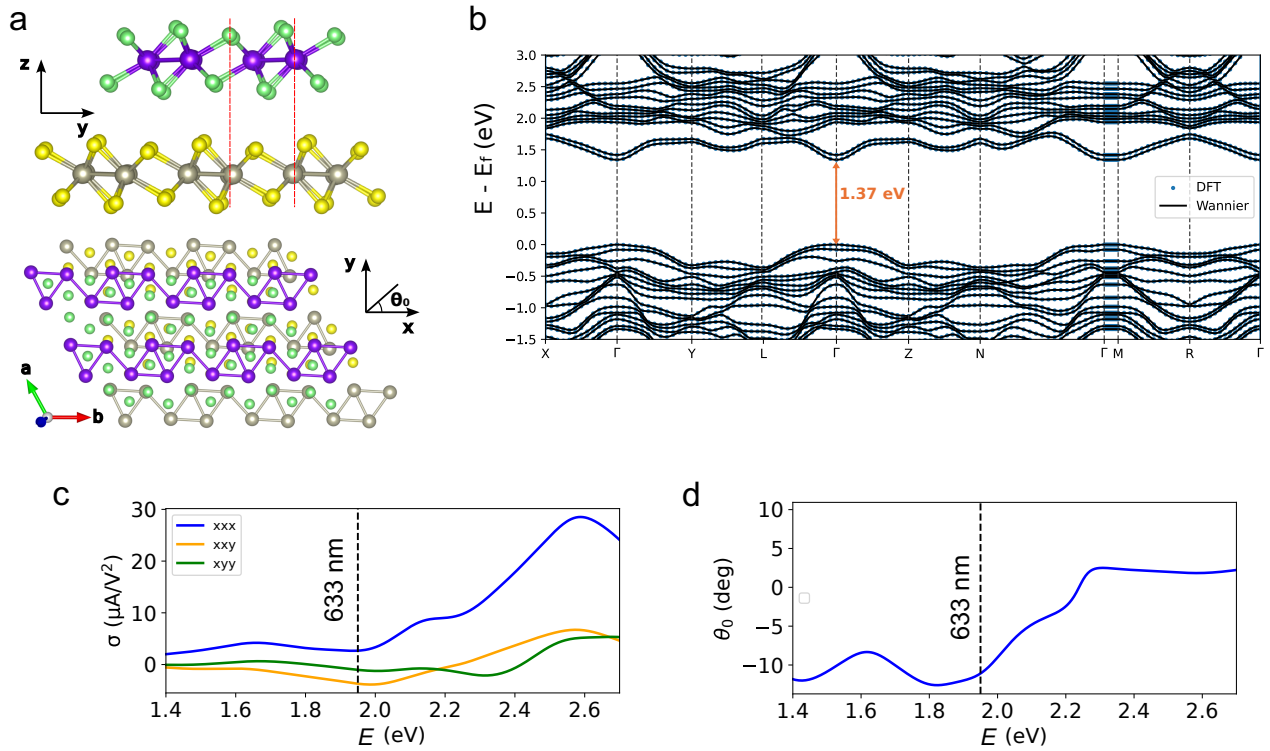


Figure 4. (a) Lattice structure of non-centrosymmetric ReS₂ bilayer. (b) Computed band structure comparing *ab-initio* and Wannierized bands. (c) Non-linear conductivity as a function of energy for all in-plane components. The dashed line corresponds to a laser wavelength of 633 nm (~ 1.95 eV) for comparison with experiment. (d) Angle of maximum photocurrent as a function of energy, which is within the range of $[-12^\circ, +2^\circ]$ relative to the b -axis for all the calculated energies.

The results are depicted in Fig. 4, where the x coordinate corresponds to the b -axis of the ReS₂ crystal and to the direction of current flow in our experiments. At 633 nm wavelength, we obtained the components $\sigma_{xxx}^{(2)} = 2.68$, $\sigma_{xyy}^{(2)} = -1.03$ and $\sigma_{xyx}^{(2)} = -3.71 \mu\text{A}/\text{V}^2$ (Fig. 4c). Our

model predicts a photocurrent with the same order of magnitude as the one observed experimentally, something noteworthy in this field.

We obtained the angle θ_0 at which photocurrent should be maximum from eq. 3 as: $\theta_0 = \frac{1}{2} \arctan 2\sigma_{xxy}^{(2)} / (\sigma_{xxx}^{(2)} - \sigma_{xyy}^{(2)})$. These results predict a maximum photocurrent at angles falling within the range of $[-12^\circ, +2^\circ]$ with respect to the b -axis of ReS₂ for all the energies computed. These angles fall within an acceptable range of $\pm 10^\circ$ angular error for our experimental setup, due to inherent limitations associated with aligning the polarization relative to the b -axis of the ReS₂ crystal.

In summary, our work unveils intrinsic BPVE in atomically thin ReS₂ through lateral device engineering. Scanning photocurrent microscopy and polarization-dependent photocurrent measurements provide compelling evidence for intrinsic photocurrent generation mechanisms. The $\sigma^{(2)}$ values extracted from experimental data are in the same order of magnitude as those obtained from theoretical calculations based on a non-centrosymmetric ReS₂ bilayer. Our device engineering strategy, combined with advanced characterization and theoretical calculations could be extended to study the intrinsic BPVE response in a broad range of non-centrosymmetric vdW materials.

ASSOCIATED CONTENT

Supporting Information. Methods; thickness estimation of ReS₂ active layers; $I_{SD} - V_{SD}$ characteristics up to 1 V; estimation of nonlinear conductivity from polarization-dependent photocurrent measurements; scanning photocurrent microscopy of a ReS₂ device with Ti/Au electrodes.

Funding Sources

ACKNOWLEDGMENT

This work has been funded by MCIN and by the European Union NextGenerationEU/PRTR-C17.I1, as well as by IKUR Strategy under the collaboration agreement between DIPC, CFM and nanoGUNE on behalf of the Department of Education of the Basque Government. This work received funding from MICIU/AEI/10.13039/501100011033 (Grant CEX2020-001038-M); from MICIU/AEI and ERDF/EU (Projects PID2021-128004NB-C21 and PID2021-

122511OB-I00); and from MICIU/AEI and European Union NextGenerationEU/PRTR (Project PCI2021-122038-2A). B.M.G. and M.G. acknowledge support from MICIU/AEI and European Union NextGenerationEU/PRTR (Grants RYC2021-034836-I and RYC2021-031705-I). B.Q.T. acknowledges support from MICIU/AEI and ESF+ (Grant PRE2022-103674). L.O.V. thanks funding from Spanish MICIU/AEI/10.13039/501100011033 and ESF+ for the PhD grant PRE2022-104385. M.R.C. is funded through grant CNS2023-145151 funded by MCIN/AEI/10.13039/501100011033 and from European Union “NextGenerationEU”/PRTR). This work has been produced using the DIPC Supercomputing Center and the Aristotle University of Thessaloniki (AUTH) High Performance Computing Infrastructure and Resources. M.R. acknowledges Roger Llopis for the LabVIEW programs and Roger Llopis and Ralph Gay for the machining of setup components. T.A. acknowledges Roger Llopis and Ralph Gay for maintenance of CIC nanoGUNE’s device fabrication facilities and financial supports from European Council via Grant agreement number 101046231 Fantasticof, and European Union via Marie Skłodowska-Curie grant agreement number 101107842 ACCESS.

ABBREVIATIONS

BPVE, bulk photovoltaic effect; CW, continuous wave; hBN, hexagonal boron nitride; vdW, van der Waals.

REFERENCES

1. Buscema, M.; Groenendijk, D. J.; Steele, G. A.; Van Der Zant, H. S., Castellanos-Gomez, A. Photovoltaic effect in few-layer black phosphorus PN junctions defined by local electrostatic gating. *Nat. Commun.* **2014**, *5*, 4651.
2. Furchi, M. M.; Pospischil, A.; Libisch, F.; Burgdorfer, J.; Mueller, T. Photovoltaic effect in an electrically tunable van der Waals heterojunction. *Nano Lett.* **2014**, *14*, 4785.
3. Ramos, M.; Gadea, M.; Mañas-Valero, S.; Boix-Constant, C.; Henríquez-Guerra, E.; Díaz-García, M. A.; Coronado, E.; Calvo, M. R. Tunable, multifunctional opto-electrical response in multilayer FePS₃/single-layer MoS₂ van der Waals p–n heterojunctions. *Nanoscale Adv.* **2024**, *6*, 1909.
4. Shockley, W.; Queisser, H. Detailed balance limit of efficiency of p-n junction solar cells. *J. Appl. Phys.* **1961**, *32*, 510.

5. Aftab, S.; Iqbal, M. Z.; Haider, Z.; Iqbal, M. W.; Nazir, G.; Shehzad, M. A. Bulk Photovoltaic Effect in 2D Materials for Solar-Power Harvesting. *Adv. Opt. Mater.* **2022**, *10*, 2201288.
6. Morimoto, T.; Nagaosa, N. Topological nature of nonlinear optical effects in solids. *Science Adv.* **2016**, *2*, e1501524.
7. Cook, A. M.; Fregoso, B. M.; De Juan, F.; Coh, S.; Moore, J. E. Design principles for shift current photovoltaics. *Nat. Commun.* **2017**, *8*, 14176.
8. Dai, Z.; Rappe, A. M. Recent progress in the theory of bulk photovoltaic effect. *Chem. Phys. Rev.* **2023**, *4*, 011303.
9. Tan, L. Z.; Zheng, F.; Young, S.M.; Wang, F.; Liu, S.; Rappe, A. M. Shift current bulk photovoltaic effect in polar materials—hybrid and oxide perovskites and beyond. *npj Comput. Mater.* **2016**, *2*, 1.
10. Koch, W. T.; Munser, R.; Ruppel, W.; Würfel, P. Bulk photovoltaic effect in BaTiO₃. *Solid State Commun.* **1975**, *17*, 847.
11. Glass, A.M.; Von der Linde, D.; Negran, T. J. High-voltage bulk photovoltaic effect and the photorefractive process in LiNbO₃. *Appl. Phys. Lett.* **1974**, *25*, 233.
12. Glass, A. M.; Von der Linde, D.; Auston, D. H.; Negran, T. J. Excited state polarization, bulk photovoltaic effect and the photorefractive effect in electrically polarized media. *J. Electron. Mater.* **1975**, *4*, 915.
13. Brody, P. S.; Crowne, F. Mechanism for the high voltage photovoltaic effect in ceramic ferroelectrics. *J. Electron. Mater.* **1975**, *4*, 955.
14. Brody, P. S. High voltage photovoltaic effect in barium titanate and lead titanate-lead zirconate ceramics. *J. Solid State Chem.* **1975**, *12*, 193.
15. Wang, M.; Wei, H.; Wu, Y.; Jia, J.; Yang, C.; Chen, Y.; Chen, X.; Cao, B. Polarization-enhanced bulk photovoltaic effect of BiFeO₃ epitaxial film under standard solar illumination. *Phys. Lett. A* **2020**, *384*, 126831.
16. Alexe, M.; Hesse, D. Tip-enhanced photovoltaic effects in bismuth ferrite. *Nat. Commun.* **2011**, *2*, 256.

17. Nadupalli, S.; Kreisel, J.; Granzow, T. Increasing bulk photovoltaic current by strain tuning. *Science Adv.* **2019**, *5*, eaau9199.
18. Ai, H.; Kong, Y.; Liu, D.; Li, F.; Geng, J.; Wang, S.; Lo, K. H.; Pan, H. 1T^{''} transition-metal dichalcogenides: strong bulk photovoltaic effect for enhanced solar-power harvesting. *J. Phys. Chem. C* **2020**, *124*, 11221.
19. Schankler, A. M.; Gao, L.; Rappe, A. M. Large bulk piezophotovoltaic effect of monolayer 2 H-MoS₂. *J. Phys. Chem. Lett.* **2021**, *12*, 1244.
20. Akamatsu, T.; Ideue, T.; Zhou, L.; Dong, Y.; Kitamura, S.; Yoshii, M.; Yang, D.; Onga, M.; Nakagawa, Y.; Watanabe, K.; Taniguchi, T. A van der Waals interface that creates in-plane polarization and a spontaneous photovoltaic effect. *Science* **2021**, *372*, 68.
21. Aftab, S.; Shehzad, M. A.; Salman Ajmal, H. M.; Kabir, F.; Iqbal, M. Z.; Al-Kahtani, A. A. Bulk photovoltaic effect in two-dimensional distorted MoTe₂. *ACS Nano* **2023**, *17*, 17884.
22. Jiang, J.; Chen, Z.; Hu, Y.; Xiang, Y.; Zhang, L.; Wang, Y.; Wang, G. C.; Shi, J. Flexo-photovoltaic effect in MoS₂. *Nature Nanotechnol.* **2021**, *16*, 894.
23. Aftab, S.; Iqbal, M. Z.; Iqbal, M. W.; Shehzad, M. A. Strain-enhanced photovoltaic effect in MoTe₂. *Laser Photonics Rev.* **2023**, *17*, 2200429.
24. Sun, R. X.; Hu, Z.; Zhao, X.; Zha, M. J.; Zhang, J.; Chen, X. D.; Liu, Z.; Tian, J. Strain-prompted giant flexo-photovoltaic effect in two-dimensional violet phosphorene nanosheets. *ACS Nano* **2024**, *18*, 13298.
25. Xin, J.; Guo, Y. Bulk photovoltaic effect in the elemental blue phosphorus-based polar homojunction and heterojunction. *J. Phys. Chem. C* **2024**, *128*, 9705.
26. Xie, X.; Leng, P.; Ding, Z.; Yang, J.; Yan, J.; Zhou, J.; Li, Z.; Ai, L.; Cao, X.; Jia, Z.; Zhang, Y. Surface photogalvanic effect in Ag₂Te. *Nat. Commun.* **2024**, *15*, 5651.
27. Quereda, J.; Ghiasi, T.S.; You, J.S.; van den Brink, J.; van Wees, B. J.; van der Wal, C.H. Symmetry regimes for circular photocurrents in monolayer MoSe₂. *Nat. Commun.* **2018**, *9*, 3346.

28. Ma, Q.; Lui, C.H.; Song, J.C.; Lin, Y.; Kong, J.F.; Cao, Y.; Dinh, T.H.; Nair, N.L.; Fang, W.; Watanabe, K.; Taniguchi, T. Giant intrinsic photoresponse in pristine graphene. *Nat. Nanotechnol.* **2019**, *14*, 145.
29. Yang, D.; Wu, J.; Zhou, B. T.; Liang, J.; Ideue, T.; Siu, T.; Awan, K. M.; Watanabe, K.; Taniguchi, T.; Iwasa, Y.; Franz, M. Spontaneous-polarization-induced photovoltaic effect in rhombohedrally stacked MoS₂. *Nat. Photonics* **2022**, *16*, 469.
30. Li, Y.; Fu, J.; Mao, X.; Chen C.; Liu H.; Gong M.; Zeng H. Enhanced bulk photovoltaic effect in two-dimensional ferroelectric CuInP₂S₆. *Nat. Commun.* **2021**, *12*, 5896.
31. Chen, X.; Xu, K.; Qin, T.; Wang, Y.; Chen, Y.; Liu, H.; Xiong, Q. Bulk photovoltaic effect in two-dimensional ferroelectric semiconductor In₂Se₃. arXiv preprint arXiv:2308.08382 **2023**.
32. Yu, J.; Huang, B.; Yang, S.; Zhang, Y.; Bai, Y.; Song, C.; Ming, W.; Liu, W.; Wang, J.; Li, C.; Wang, Q. Flexoelectric Engineering of Bulk Photovoltaic Photodetector. *Nano Lett.* **2024**, *24*, 6337.
33. Nahid, S.M.; Nam, S.; van der Zande, A. M. Depolarization field-induced photovoltaic effect in graphene/ α -In₂Se₃/graphene heterostructures. *ACS Nano* **2024**, *18*, 14198.
34. Wildervanck, J.C.; Jellinek, F. The dichalcogenides of technetium and rhenium. *J. Less-Common Met.* **1971**, *24*, 73.
35. Lamfers, H. J.; Meetsma, A.; Wiegers, G. A.; De Boer, J. L. The crystal structure of some rhenium and technetium dichalcogenides. *J. Alloys Compd.* **1996**, *241*, 34.
36. Rahman, M.; Davey, K.; Qiao, S. Z. Advent of 2D rhenium disulfide (ReS₂): fundamentals to applications. *Adv. Funct. Mater.* **2017**, *27*, 1606129.
37. Qiao, X. F.; Wu, J. B.; Zhou, L.; Qiao, J.; Shi, W.; Chen, T.; Zhang, X.; Zhang, J.; Ji, W.; Tan, P. H. Polytypism and unexpected strong interlayer coupling in two-dimensional layered ReS₂. *Nanoscale* **2016**, *8*, 8324.
38. Song, Y.; Hu, S.; Lin, M. L.; Gan, X.; Tan, P. H.; Zhao, J. Extraordinary second harmonic generation in ReS₂ atomic crystals. *ACS Photonics* **2018**, *5*, 3485.

39. Wan, Y.; Hu, T.; Mao, X.; Fu, J.; Yuan, K.; Song, Y.; Gan, X.; Xu, X.; Xue, M.; Cheng, X.; Huang, C. Room-temperature ferroelectricity in 1T'-ReS₂ multilayers. *Phys. Rev. Lett.* **2022**, *128*, 067601.
40. Zhou, Y.; Zhou, X.; Yu, X. L.; Liang, Z.; Zhao, X.; Wang, T.; Miao, J.; Chen, X. Giant intrinsic photovoltaic effect in one-dimensional van der Waals grain boundaries. *Nat. Commun.* **2024**, *15*, 501.
41. Liang, Z.; Zhou, X.; Zhang, L.; Yu, X. L.; Lv, Y.; Song, X.; Zhou, Y.; Wang, H.; Wang, S.; Wang, T.; Shum, P. P. Strong bulk photovoltaic effect in engineered edge-embedded van der Waals structures. *Nat. Commun.* **2023**, *14*, 4230.
42. Wang, J.; Han, N.; Lin, Z.; Hu, S.; Tian, R.; Zhang, M.; Zhang, Y.; Zhao, J.; Gan, X. A giant intrinsic photovoltaic effect in atomically thin ReS₂. *Nanoscale* **2024**, *16*, 3101.
43. Wang, W.; Xiao, Y.; Li, T.; Lu, X.; Xu, N.; Cao, Y. Piezo-photovoltaic Effect in Monolayer 2H-MoS₂. *J. Phys. Chem. Lett.* **2024**, *15*, 3549.
44. Dong, Y.; Yang, M. M.; Yoshii, M.; Matsuoka, S.; Kitamura, S.; Hasegawa, T.; Ogawa, N.; Morimoto, T.; Ideue, T.; Iwasa, Y. Giant bulk piezophotovoltaic effect in 3R-MoS₂. *Nat. Nanotechnol.* **2023**, *18*, 36.
45. Lin, Y. C.; Komsa, H. P.; Yeh, C. H.; Bjorkman, T.; Liang, Z. Y.; Ho, C. H.; Huang, Y. S.; Chiu, P. W.; Krasheninnikov, A. V.; Suenaga, K. Single-layer ReS₂: two-dimensional semiconductor with tunable in-plane anisotropy. *ACS Nano* **2015**, *9*, 11249.
46. Intonti, K.; Faella, E.; Kumar, A.; Viscardi, L.; Giubileo, F.; Martucciello, N.; Lam, H. T.; Anastasiou, K.; Craciun, M.; Russo, S.; Di Bartolomeo, A. Temperature-dependent conduction and photoresponse in few-layer ReS₂. *ACS Appl. Mater. Inter.* **2023**, *15*, 50302.
47. Park, J. Y.; Joe, H. E.; Yoon, H. S.; Yoo, S.; Kim, T.; Kang, K.; Min, B. K.; Jun, S. C. Contact effect of ReS₂/metal interface. *ACS Appl. Mater. Inter.* **2017**, *9*, 26325.
48. Akatsuka, S.; Sakano, M.; Yamamoto, T.; Nomoto, T.; Arita, R.; Murata, R.; Sasagawa, T.; Watanabe, K.; Taniguchi, T.; Mitsuishi, N.; Kitamura, M. 180°-twisted bilayer ReSe₂ as an artificial noncentrosymmetric semiconductor. *Phys. Rev. Res.* **2024**, *6*, L022048.

49. Ibañez-Azpiroz, J.; Tsirkin, S. S.; Souza, I. Ab initio calculation of the shift photocurrent by Wannier interpolation. *Phys. Rev. B* **2018**, *97*, 245143.

Supporting Information

Contents

1. Methods
2. Thickness estimation of ReS₂ active layers
3. $I_{SD} - V_{SD}$ characteristics up to 1 V
4. Estimation of nonlinear conductivity from polarization-dependent photocurrent measurements
5. Scanning photocurrent microscopy of a ReS₂ device with Ti/Au electrodes

1. Methods

Device fabrication. Commercially available ReS₂ and hBN crystals were obtained from HQ Graphene, while the graphite crystals were sourced from NGS Naturgraphit GmbH. Each type of crystal was separately exfoliated on freshly cleaned SiO₂/Si substrates using the mechanical cleavage technique. ReS₂ flakes with a thickness of 2-10 layers and graphite flakes with a thickness of 4-5 layers were identified via optical contrast, and hBN flakes with a thickness of 20-40 nm were also identified. To fabricate the encapsulated graphene-contacted ReS₂ device, we used dry pick-up and transfer techniques as previously described in the literature (1-3). The exfoliation and dry transfer were performed inside an Ar-filled glovebox. We employed a drop of transparent LCC polymer (Lakme Colour Crush by Lakme India) as a sacrificial polymer (SP) layer. The convex meniscus of the SP was used to pick up the top hBN layer. Subsequently, two graphite layers were picked up one by one beneath the top hBN layer, aligned parallel to each other with approximately 10 μm distance. Next, the ReS₂ and bottom hBN were picked up to complete the heterostructure. All pick-ups were performed at ~ 60°C. The SP, along with the heterostructure, was then placed on a freshly cleaned 300 nm p⁺⁺-SiO₂/Si chip at ~ 100°C. The chip was immersed in a 1:3 acetone: IPA solution overnight to dissolve the SP, leaving a clean encapsulated heterostructure on the chip. Standard e-beam lithography was used to design the electrical leads. Reactive ion etching (RIE) was applied to selected areas of the hBN-encapsulated graphite to metallize on the graphite contacts. The RIE process, utilizing SF₆ gas at a flow rate of 20 sccm, a pressure of 20 mTorr, and an RF power of 35 W for approximately 15 seconds, etched away the top hBN. It is worth noting that the SF₆ RIE recipe etches hBN 90 times faster than graphene, effectively stopping at the graphite layer. Following this, 5/50 nm Ti/Au electrodes were evaporated to create metal contacts to complete the device.

μ-Raman spectroscopy. A Renishaw in Via Qontor microscope was used to characterize the Raman spectra of the samples at room temperature using a 532-nm CW laser as the excitation source. A 50× focusing objective providing a laser spot size of ~1 μm was used during data acquisition. To investigate the polarization dependence of the Raman modes, the samples were rotated relative to the polarization direction of the incident laser.

Atomic force microscopy. To study the thickness and topography of the devices, an AFM microscope (Bruker) was used in non-contact mode with a standard tip and in ambient conditions. Scanning speeds equal to or lower than 0.6 lines/s were used during acquisition for better quality imaging.

Photocurrent measurements and scanning photocurrent microscopy. Photocurrent measurements were performed as an extended home-built setup of a Renishaw in Via Qontor Raman microscope. The instrument's 532-nm and 633-nm CW excitation sources were employed for photoexcitation within a power range of 10 – 300 μ W. The devices were mounted onto a commercial cryostat (Linkam, HFS350EV-PB4) provided of an optical window and electrical connections. The optical window provided both Raman spectroscopy and photocurrent measurements simultaneously. Electrical contacts were established via wire bonding for photocurrent detection using a Keithley 2634B sourcemeter. To study the polarization dependence of the photocurrent, a half-wave plate was inserted in the optical path prior to the focusing objective. The half-wave plate was then rotated relative to the incident laser polarization. Scanning photocurrent microscopy was conducted using the same experimental setup. During this measurement, a tightly focused laser beam ($\sim 1 \mu\text{m}$ diameter) was used to illuminate the different areas of the device while scanning the sample and the photocurrent generated at each position was measured. All photocurrent measurements were conducted in ambient conditions.

Activation energy. The activation energy of the devices was determined from temperature-dependent $I_{\text{DS}}-V_{\text{DS}}$ measurements in the temperature range of 80 to 300 K, with a step size of 20 K (see Fig. S1), and with a stabilization time of 12 minutes before each measurement. To do this, the devices were placed in a commercial cryostat (Linkam, HFS350EV-PB4) with a liquid nitrogen flux and using the same electronic components as for photocurrent measurements. The activation energy was then extracted from the variation of the channel conductance with temperature at $V_{\text{DS}} = 0.1 \text{ V}$, which is given by the equation $G(T) = G_0 e^{-E_a/K_b T}$, corresponding to the slope of the Arrhenius plot.

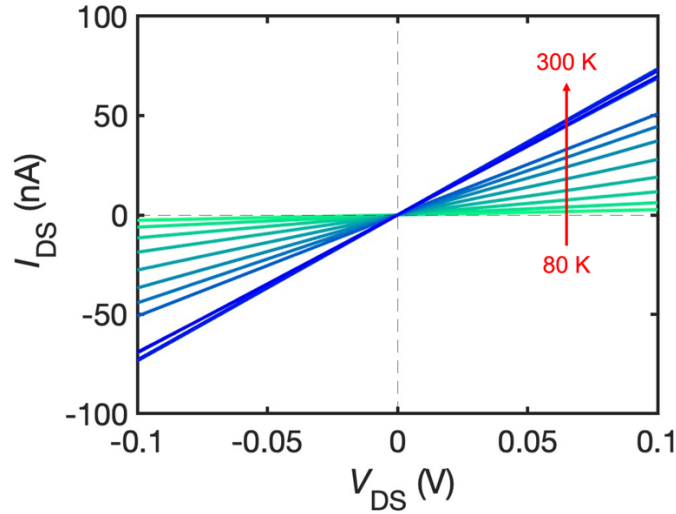


Figure S5. Temperature-dependent $I_{DS} - V_{DS}$ curves of a bilayer ReS_2 device, in the temperature range of 80 to 300 K with a step size of 20 K.

First principles simulations. Since in the $1T'$ structure there is an inversion center at the center of the 4-Re cluster, stacking two identical copies with an arbitrary lateral shift between them leads to a new inversion center exactly in between the original (intralayer) inversion centers.

The simulated structure was derived from the AB stacking phase of bilayer ReS_2 (4), where each monolayer has inversion symmetry, and the top layer is rotated 180° with respect to the center of inversion on the xy plane, while the atoms of the top layer are displaced on the same plane to the non-inversion symmetric minimum phase (5).

ReS_2 was simulated using QuantumEspresso (6-7). Non-spin-polarized simulations were performed. Optimized, norm-conserving, scalar relativistic pseudopotential with a Perdew–Burke–Ernzerhof exchange–correlation functional were employed (8-9). A wavefunction cut-off 90 Ry was used with a k -point grid of $9 \times 9 \times 1$. vdW interactions were considered using the DFT-D3 model. The bilayer, inversion symmetric structure was originally relaxed to the point that the forces on ions were below 2×10^{-6} Ha/bohr ($0.1 \text{ meV}/\text{\AA}$). The resulting in-plane lattice constants are $a = 6.49$ and $b = 6.38 \text{ \AA}$. The distance between two Re atoms along the z axis was $\sim 6.2 \text{ \AA}$, which agrees with calculations of the bulk primitive structure, with the use of vdW interactions that resulted in a c lattice constant of 6.21 \AA . Overall, these values are in good agreement with previous theoretical (10) and experimental results (11). The AB

structure was then derived from this relaxed bilayer structure and the atoms of the top layer were displaced on the xy plane, so as to arrive approximately at the A' state, which is described in Ref. (5). A final relaxation step was performed, which slightly moved the atoms of the top layer to their minimum at the A' position ($\sim 0.1 \text{ \AA}$ on each cartesian direction). It was also ensured that in the relaxed structure the b lattice vector was aligned with the x axis.

Projected Wannier functions were constructed for the bilayer ReS_2 in state A' using Wannier90 (12). A frozen energy window was added for all valence bands and up to $\sim 3 \text{ eV}$ from the highest occupied valence band. The $\text{Re}(d)$ and $\text{S}(p)$ orbitals were used as the basis set. WannierBerri was used for the shift current calculations (13). A grid of $150 \times 150 \times 28$ was used. The parameter used for the regularization procedure to avoid near degeneracies in the sum-over-states was set to $\eta = 0.04 \text{ eV}$ and a fixed Lorentzian broadening width of 0.1 eV was used.

2. Thickness estimation of ReS₂ active layers

μ -Raman spectroscopy

μ -Raman spectroscopy was employed to accurately characterize the thickness of the atomically thin ReS₂ flakes composing our two devices exhibiting intrinsic BPVE. Previous studies have established that Raman spectroscopy can effectively distinguish the thickness of ReS₂, particularly for very few-layer structures, by analyzing the difference between vibrational modes III (~ 150 cm⁻¹) and I (~ 136 cm⁻¹) (see Ref. (14)).

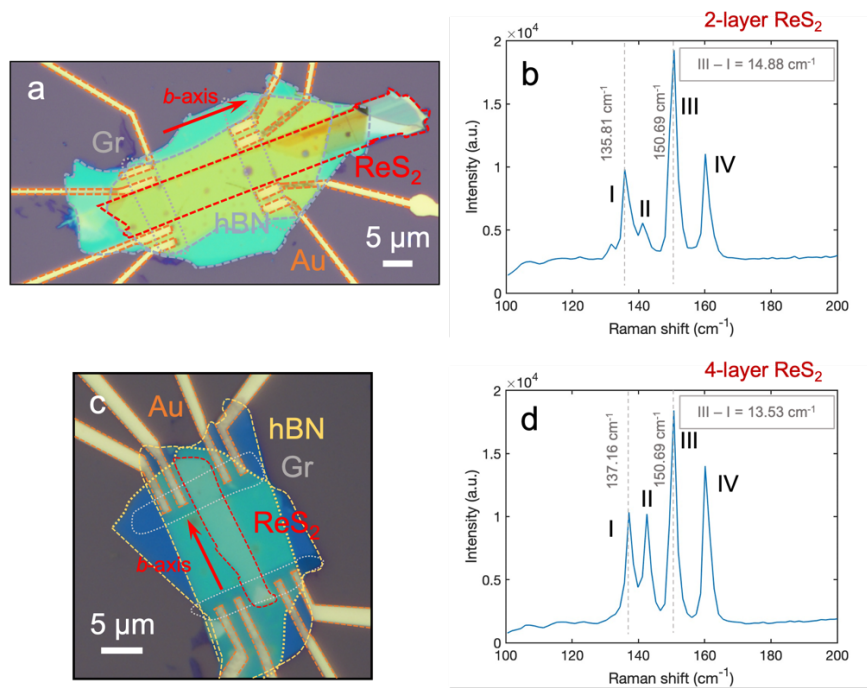


Figure S6. (a) Optical image of device A. (b) Raman spectrum of device A obtained from the active ReS₂ channel. The frequency difference between modes III and I is 14.88 cm⁻¹, in agreement with a bilayer ReS₂ flake. (c) Optical image of device B. (d) Raman spectrum of device B obtained from the center of the active ReS₂ channel. The difference between vibrational modes III and I is 13.53 cm⁻¹, revealing a four-layer ReS₂ flake.

Fig. S2 presents optical images of the two fabricated devices (device A, characterized in Fig. 2, and device B, characterized in Fig. 3 of the main manuscript) and representative Raman spectra for each of them within the frequency range of 100 – 200 cm⁻¹. For each device, three Raman spectra were acquired at different locations within the ReS₂ active channel. The

calculated frequency difference between modes III and I remained constant for all the three spectra obtained from individual devices. The results are summarized in Fig. S2(b), (d).

By comparing these values with those reported in previous studies (14), we were able to accurately estimate the thickness of device *A* as a two-layer ReS₂ flake and device *B* as a four-layer ReS₂ flake.

Optical color contrast

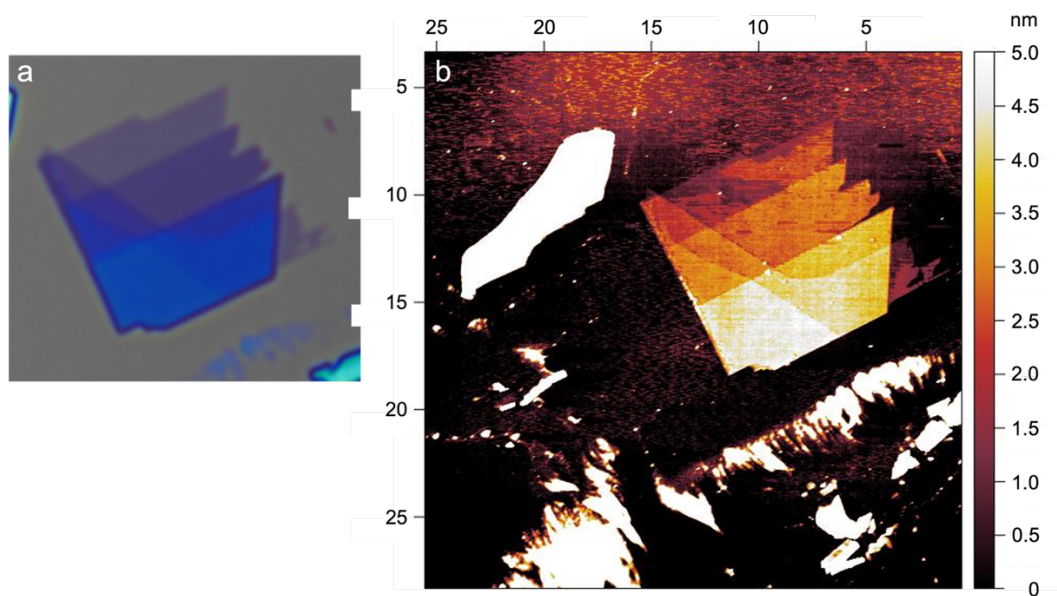








Figure S7. (a) Optical image of a ReS₂ flake with different thicknesses onto a SiO₂ substrate. (b) Atomic force microscope image of the flake shown in panel a.

Table S1. Optical color contrast and its corresponding number of ReS₂ layers obtained from the data in Fig. S3.

Color	# of layers
	7
	6
	5
	4
	3
	2
	1
	SiO ₂

Following the guideline in Table S1, we could have a rough estimation of the thickness of the desired ReS₂ flakes before proceeding with the device fabrication.

Atomic force microscopy

As a complementary thickness characterization technique, we performed atomic force microscopy (AFM) measurements of the two devices showing BPVE several months after their fabrication and BPVE characterization. During this time, the devices were exposed to air and the AFM measurements might be affected by the accumulation of dust and other contaminants on the surface. Additionally, the presence of the hBN encapsulation introduced challenges in accurately determining the thickness of the underlying ReS₂ flake, which can lead to an overestimation of the flake thickness in case of small air gaps or surface contaminants deposited after several months from device fabrication. Nevertheless, we provide these results in Fig. S4 and Fig. S5.

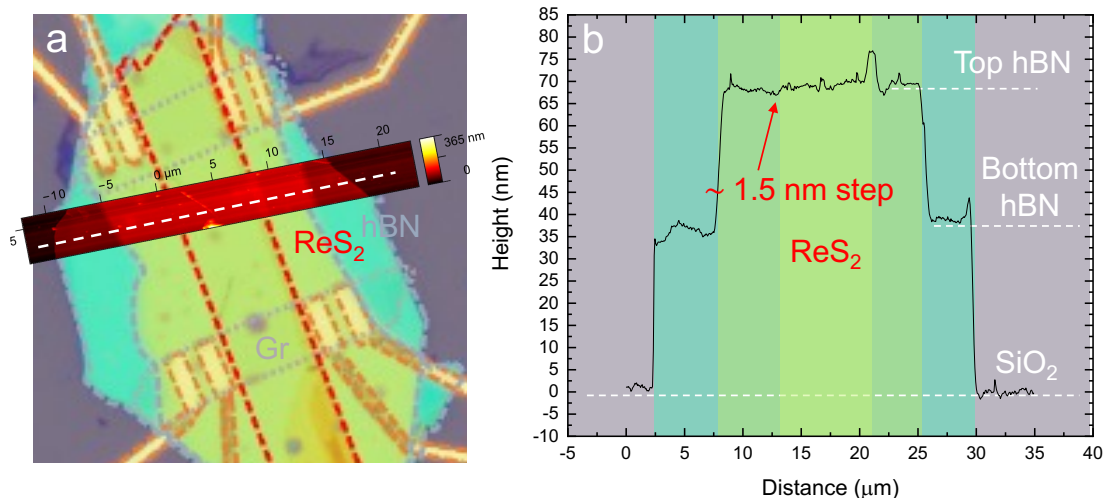


Figure S8. (a) Optical image of device *A* (characterized in Fig. 2 of the main manuscript) with an overlaid AFM image of the corresponding area. (b) Transverse line profile from the AFM image in panel a, extracted from the dashed white line. Here, the ReS_2 layer has a thickness of ~ 1.5 nm.

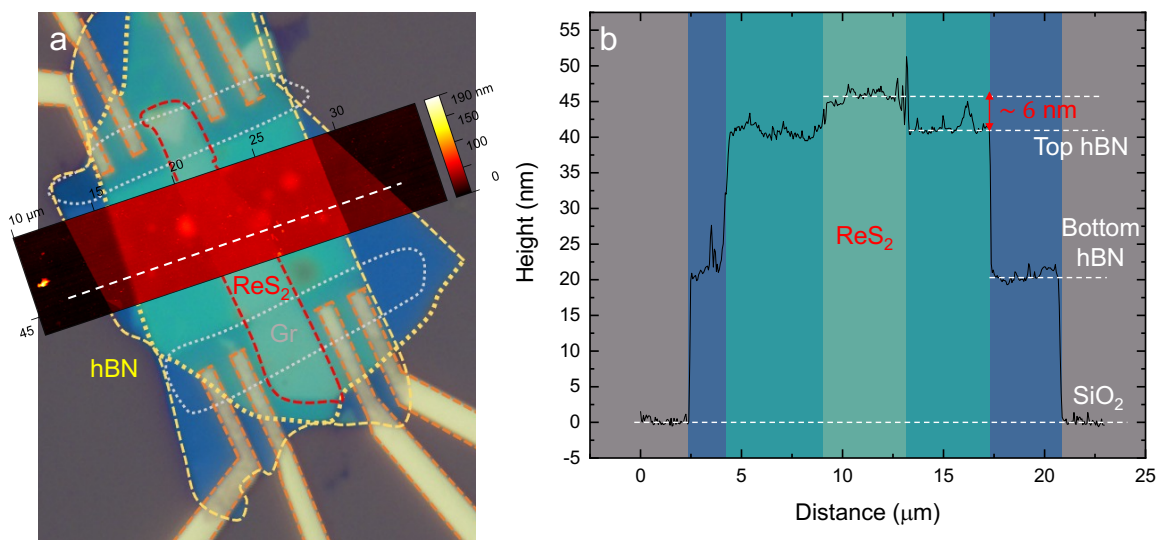


Figure S9. (a) Optical image of device *B* (characterized in Fig. 3 of the main text) with an overlaid AFM image of the corresponding device area. (b) Transverse device line profile extracted from the dashed white line in panel a. Here, the active ReS_2 channel has an approximated thickness of about 5 to 6 nm.

The thickness estimate obtained from AFM for the device in Fig. S5 does not align with the thickness derived from Raman spectroscopy (Fig. S2 (d)). Based on the consistency and

accuracy of Raman spectroscopy in measuring ReS₂ thickness at its few-layer limit, we consider the Raman-derived values to be the most trustworthy.

3. $I_{SD} - V_{SD}$ characteristics up to 1 V

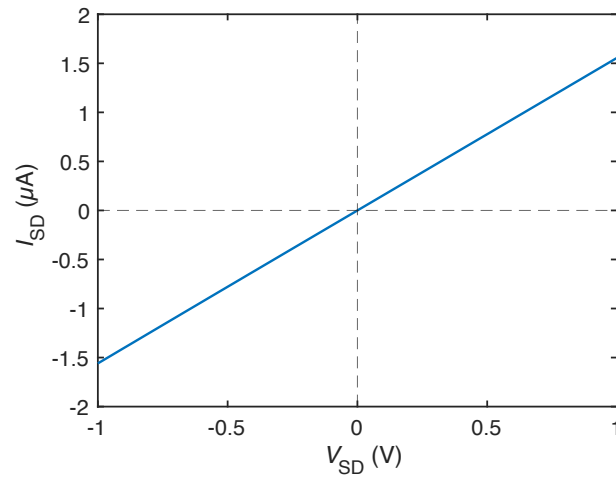


Figure S6. Output curve of a representative ReS_2 device with graphite contacts under dark conditions.

4. Estimation of nonlinear conductivity from polarization-dependent photocurrent measurements

Non-centrosymmetric materials can exhibit a second-order photocurrent response. Under linearly polarized light, a photocurrent density j_i along the i direction can be generated:

$$j_i^{\text{BPVE}} = \sigma_{ijk}^{(2)} E_j E_k \quad (\text{S1})$$

Here, $\sigma_{ijk}^{(2)}$ is the nonlinear conductivity, and E_j , E_k are the electric fields applied along j and k directions, which in our case correspond to the electric field of the incoming light wave or light polarization direction.

$\sigma_{ijk}^{(2)}$ is a third-rank tensor that captures the material's ability to conduct current in response to a second-order electric field dependence. Due to its tensorial nature, it can be expressed in a matrix form to account for all possible combinations of electric field components:

$$\begin{pmatrix} j_x \\ j_y \\ j_z \end{pmatrix} = \begin{pmatrix} \sigma_{xxx}^{(2)} & \sigma_{xyy}^{(2)} & \sigma_{xzz}^{(2)} & \sigma_{xyz}^{(2)} & \sigma_{xxz}^{(2)} & \sigma_{xxy}^{(2)} \\ \sigma_{yxx}^{(2)} & \sigma_{yyy}^{(2)} & \sigma_{yzz}^{(2)} & \sigma_{yyz}^{(2)} & \sigma_{yxz}^{(2)} & \sigma_{yyx}^{(2)} \\ \sigma_{zxx}^{(2)} & \sigma_{zyy}^{(2)} & \sigma_{zzz}^{(2)} & \sigma_{zyz}^{(2)} & \sigma_{zxz}^{(2)} & \sigma_{zxy}^{(2)} \end{pmatrix} \begin{pmatrix} E_x E_x \\ E_y E_y \\ E_z E_z \\ 2E_y E_z \\ 2E_x E_z \\ 2E_x E_y \end{pmatrix} \quad (\text{S2})$$

Since few-layer ReS_2 breaks all symmetries, all the tensorial elements of $\sigma_{ijk}^{(2)}$ are non-zero. However, in our experiments, both the electric field (or light polarization) and the photocurrent detection are restricted to an in-plane configuration. Consequently, elements like those describing current flow along the z -axis can be disregarded. Also, since the photocurrent detection takes place along the b -axis of ReS_2 , we adopt a convention where the b -axis aligns with the x -coordinate direction of our experimental setup. Therefore, the equation describing the photocurrent density simplifies to:

$$j_x = \sigma_{xxx}^{(2)} E_x^2 + \sigma_{xyy}^{(2)} E_y^2 + 2\sigma_{xxy}^{(2)} E_x E_y \quad (\text{S3})$$

Since photocurrent is directly measured during experiments, we can express eq. S3 in terms of photocurrent as:

$$I_x = t \cdot r (\sigma_{xxx}^{(2)} E_x^2 + \sigma_{xyy}^{(2)} E_y^2 + 2\sigma_{xxy}^{(2)} E_x E_y) \quad (\text{S4})$$

where t is the thickness of the ReS₂ channel and r is the laser beam radius. This approach assumes that the photocurrent is primarily generated within the area illuminated by the laser beam.

Considering an electric field amplitude E_0 forming an angle θ with respect to the x -axis, then E_x and E_y can be written as $E_x = E_0 \cos \theta$ and $E_y = E_0 \sin \theta$. Substituting these expressions into eq. S4, we obtain:

$$I_x = t \cdot r \cdot E_0^2 (\sigma_{xxx}^{(2)} \cos^2 \theta + \sigma_{xyy}^{(2)} \sin^2 \theta + 2\sigma_{xxy}^{(2)} \cos \theta \sin \theta) \quad (\text{S5})$$

For a monochromatic propagating wave, the light intensity is related to the electric field amplitude as:

$$I_{\text{opt}} = \frac{1}{2} c \varepsilon_0 n |E_0|^2 \quad (\text{S6})$$

where c is the speed of light, ε_0 is the vacuum permittivity and n is the refractive index of ReS₂.

Also, for a Gaussian beam with optical power P_{opt} and beam radius r , the optical intensity can be written as:

$$I_{\text{opt}} = \frac{2P_{\text{opt}}}{\pi r^2} \quad (\text{S7})$$

Substituting expressions S6 and S7 into eq. S5, then the photocurrent can be written as a function of the optical power:

$$I_x = 4 \frac{t \cdot P_{\text{opt}}}{\pi c \varepsilon_0 r} (\sigma_{xxx}^{(2)} \cos^2 \theta + \sigma_{xyy}^{(2)} \sin^2 \theta + 2\sigma_{xxy}^{(2)} \cos \theta \sin \theta) \quad (\text{S8})$$

The previous equation has been used to fit the polarization-dependent photocurrent shown in Fig. 2d of the main text. The fitting was performed using the following parameter values: $t = 1.56$ nm (corresponding to a bilayer ReS₂ active channel), $P_{\text{opt}} = 120$ μW , $n = 4.6$ (at 633 nm wavelength, obtained from Ref. (15)) and $r = 0.5$ μm .

The nonlinear conductivity values for a bilayer ReS₂ obtained from this fit are: $\sigma_{xxx}^{(2)} = 5.51$ $\mu\text{A}/\text{V}^2$, $\sigma_{xyy}^{(2)} = 3.06$ $\mu\text{A}/\text{V}^2$ and $\sigma_{xxy}^{(2)} = -0.05$ $\mu\text{A}/\text{V}^2$. The *R*-square value of the fit is 0.98.

5. Scanning photocurrent microscopy of a ReS₂ device with Ti/Au contacts

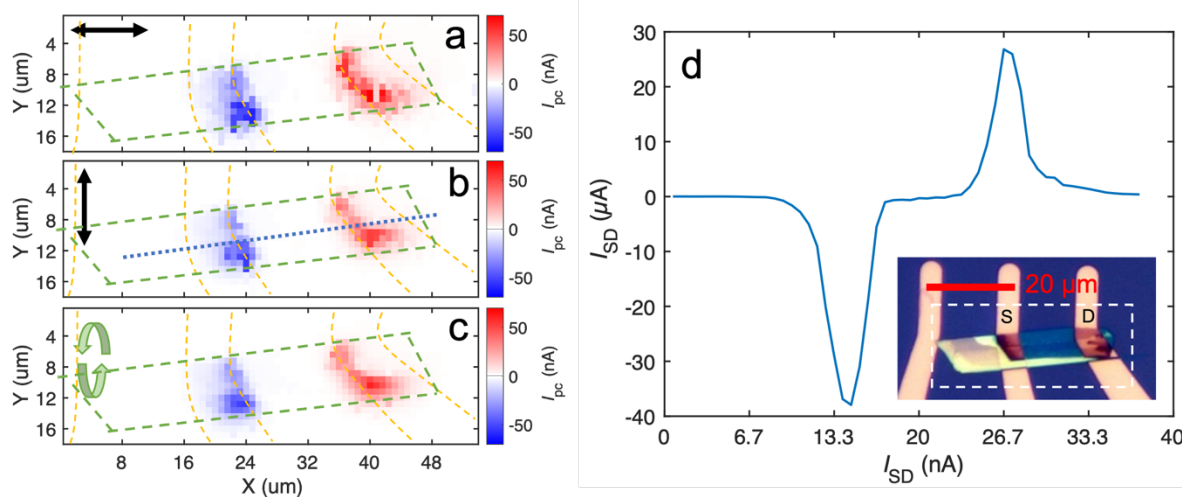


Figure S7. (a) – (c) Scanning photocurrent maps at 532-nm wavelength of a ReS₂ flake with different few-layer thicknesses and contacted to Ti/Au electrodes. The power used for all SPCM maps is 400 μW . The light polarization is indicated at the top-left corner of each map. (d) Longitudinal line profile obtained from the SPCM map shown in panel (b). The inset shows a microscopic image of the sample, where *S* and *D* denote the source and drain contacts.

Supplementary references

1. *Deterministic transfer of two-dimensional materials by all-dry viscoelastic stamping.* **A. Castellanos-Gomez, et al.** 1, 2014, 2D Materials, Vol. 1, p. 011002.
2. *Number-Resolved Single-Photon Detection with Ultralow Noise van der Waals Hybrid.* **K. Roy, et al.** 2, 2018, Advanced Materials, Vol. 30, p. 1704412.
3. *Thermal history-dependent current relaxation in hBN/MoS₂ van der Waals dimers.* **T. Ahmed, et al.** 5, 2020, ACS nano, Vol. 14, pp. 5909-5916.
4. *Non-synchronous bulk photovoltaic effect in two-dimensional interlayer-sliding ferroelectrics.* **R. C. Xiao, et al.** 1, 2022, npj Computational Materials, Vol. 8, p. 138.
5. *Room-Temperature Ferroelectricity in 1 T'-ReS₂ Multilayers.* **Y. Wan, et al.** 6, 2022, Physical Review Letters, Vol. 128, p. 067601.
6. *QUANTUM ESPRESSO: a modular and open-source software project for quantum simulations of materials.* **P. Giannozzi, et al.** 39, 2009, Journal of physics: Condensed matter, Vol. 21, p. 395502.
7. *Advanced capabilities for materials modelling with Quantum ESPRESSO.* **P. Giannozzi, et al.** 46, 2017, Journal of physics: Condensed matter, Vol. 29, p. 465901.
8. *The PseudoDojo: Training and grading a 85 element optimized norm-conserving pseudopotential table.* **M. J. Van Setten, et al.** 2018, Computer Physics Communications, Vol. 226, pp. 39-54.
9. *Optimized norm-conserving Vanderbilt pseudopotentials.* **Hamann, D. R.** 8, 2013, Physical Review B, Vol. 88, p. 085117.
10. *Theoretical investigations of the anisotropic optical properties of distorted 1T ReS₂ and ReSe₂ monolayers, bilayers, and in the bulk limit.* **J. P. Echeverry, et al.** 7, 2018, Physical Review B, Vol. 97, p. 075123.
11. *Structure of rhenium disulfide.* **H. H. Murray, et al.** 19, 1994, Inorganic Chemistry, Vol. 33, pp. 4418-4420.

12. *An updated version of wannier90: A tool for obtaining maximally-localised Wannier functions.* **A. A. Mostofi, et al.** 8, 2014, Computer Physics Communications, Vol. 185, pp. 2309-2310.
13. *High performance Wannier interpolation of Berry curvature and related quantities with WannierBerri code.* **Tsirkin, S.S.** 1, 2021, npj Computational Materials, Vol. 7, p. 33.
14. *In-plane anisotropy in mono- and few-layer ReS₂ probed by Raman spectroscopy and scanning transmission electron microscopy.* **D. A. Chenet, et al.** 9, 2015, Nano Letters, Vol. 15, pp. 5667.
15. Refractive index database. <https://refractiveindex.info/> (accessed 2024-07-22).